ADVANCED FUNCTIONAL MATERIALS

www.afm-journal.de

Batteries

By controlling and optimizing the formulation of a composite electrode and the sintering parameters (temperature, pressure), which affect compactness of both the electrolyte and the composite electrode, an efficient and safe monolithic solid-state Li-ion battery can be assembled in a one-step process by spark plasma sintering (SPS). On page 2140, Renaud Bouchet and co-workers report that the first prototype shows good cycling and promising electrochemical performance.

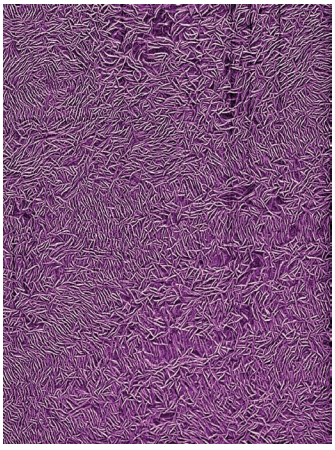

Nanoporous Membranes

Molecular entangling of polymeric chains is considered a negative characteristic that restricts crystallization and results in inferior physical properties. On page 2048, Hiroki Uehara and co-workers demonstrate that using melt-drawing and subsequent melt-shrinking techniques allows for control of the entanglement positions of ultrahigh molecular weight polyethylene, resulting in a homogeneous lamellar morphology, similar to block copolymers. Such entanglement control also enables the preparation of nanoporous, but large-area, membranes without any solvent processing.

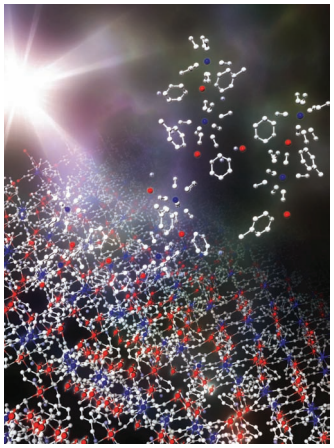

Magnetic Materials

As reported by Shin-ichi Ohkoshi and co-workers on page 2089 a three-dimensional Co-W bimetallic assembly possessing two different aromatic molecules, $[\{Co^{II}(4\text{-methylpyridine})(pyrimidine)\}_2\{Co^{II}(H_2O)_2\}\{W^{V}(CN)_8\}_2]\cdot 4H_2O$, exhibits a photoinduced magnetization due to an optical charge-transfer-induced spin transition with a high Curie temperature (T_C) of 48 K and a gigantic coercive field (H_C) of 27 000 Oe. The T_C and H_C values are the highest reported for photoinduced magnetization systems.

CONTENTS

FEATURE ARTICLE

Biomimetics

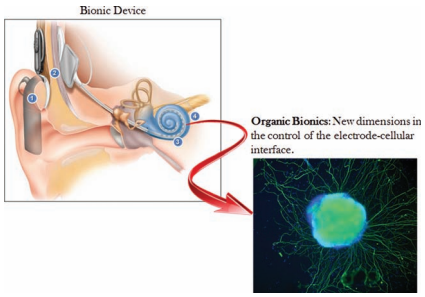

Advances in medical bionics technology are dependent upon eliciting precise control of biological events at the electrode/cellular interface. The advent of carbon-based organic conductors now provides the platform for unprecedented possibilities. These organic conductors are inherently cytocompatible and the ability to precisely control interfacial chemistries through electrical stimulation brings new dimensions to bionic devices.

FULL PAPERS

Self-Assembly

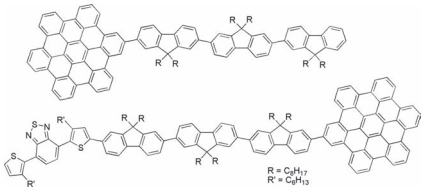

A series of solution processable mono- and bis-substituted hexa-*peri*-hexabenzocoronene (HBC) derivatives are prepared and fully characterized. The fluorenyl hexa-*peri*-hexabenzocoronene (FHBC) compounds show strong intermolecular associations in both solution and the solid state. The attachment of organic dye units broadens the absorption of the HBC compounds and improves their performance in bulk heterojunction solar cells applications.

Tissue Engineering

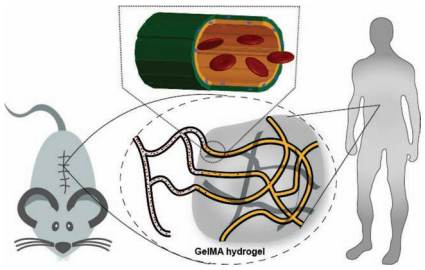

Using gelatin methacrylate (GelMA) hydrogel as the embedding scaffold, 3D constructs containing human-blood-derived endothelial colony-forming cells (ECFCs) and bone marrow-derived mesenchymal stem cells (MSCs) are shown to generate extensive, functional capillary-like networks in vitro and in vivo. These data suggest that GelMA hydrogels can be used for biomedical applications requiring the formation of microvascular networks, including development of complex engineered tissues.

Light-Emitting Diodes

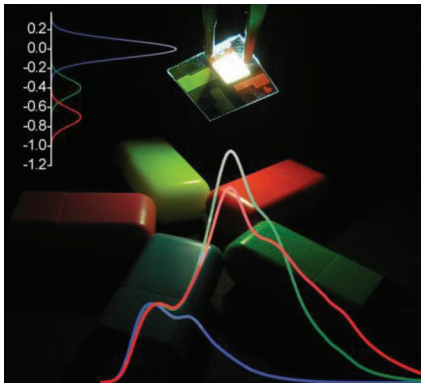

The device operation of a single-layer white-emitting polymer light-emitting diode (PLED) is investigated. From single-carrier devices it is determined that the red and green dyes act as electron traps. Taking into account trap-assisted recombination on the dyes and Langevin recombination on the blue backbone, the color shift of the white-emitting PLEDs can be explained.

FULL PAPERS

Nanowrinkled polyethylene membranes with a network of 30 nm-thick homogeneous lamellae are prepared using a novel entanglement control technique composed of biaxial melt-drawing and melt-shrinking procedures. Subsequent cold-drawing causes delamination of the lamellar interfaces, leading a nanoporous morphology composed of passing-through channels several tens of nanometers in diameter without any solvent processing.

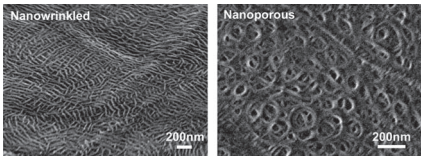

Polarization responses of different disordered ferroelectrics are shown to exhibit universal scaling properties, which support the hypothesis that the response of the different materials is dominated by the statistical electric field distributions rather than by distinct microscopic switching mechanisms. These field distributions, which result in broad switching time spectra, can be directly obtained from the logarithmic field derivatives of the polarization.

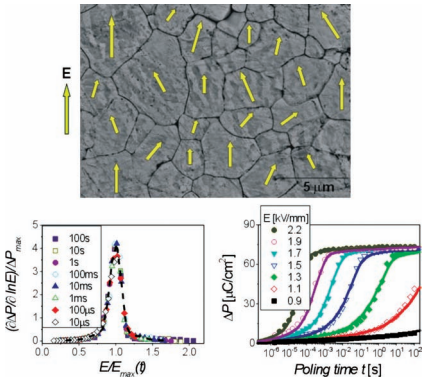

Surface-enhanced Raman scattering substrates are fabricated based on the silicon–hydrogen bond assembly of Cu nanoparticles on silicon wafers. These substrates show excellent enhanced effects and visible uniformity in the detection of rhodamine 6G and sudan I with a relative standard deviation (RSD) of <20%. A possible explanation for the enhancement and uniformity is proposed.

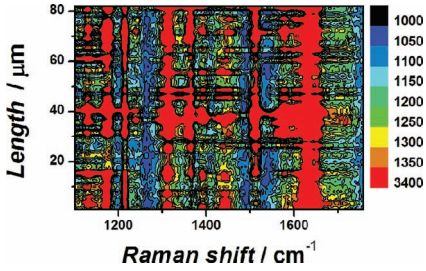

A scheme for the overall synthesis process of the magnetophotonic crystal MPC-Fe_3O_4 is presented. First, pretreated butterfly wings are immersed into a ferric chloride sol solution, allowing a sol-gel coating process. Then the biotemplate is removed at an elevated temperature, producing the hematite photonic crystal structure (PC-α-Fe_2O_3). Finally, the reduction of the PC-α-Fe_2O_3 in H_2/Ar results in the magnetophotonic crystal structure (MPC-Fe_3O_4).

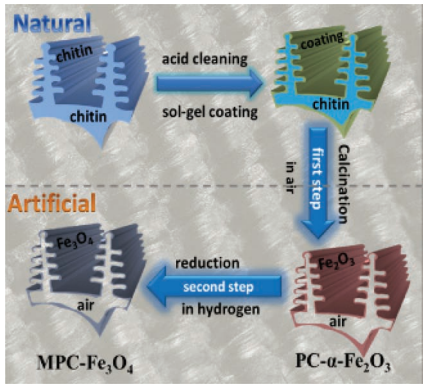

CONTENTS

FULL PAPERS

Nanocrystals

Highly Emissive and Color-Tunable $CuInS_2$-Based Colloidal Semiconductor Nanocrystals: Off-Stoichiometry Effects and Improved Electroluminescence Performance

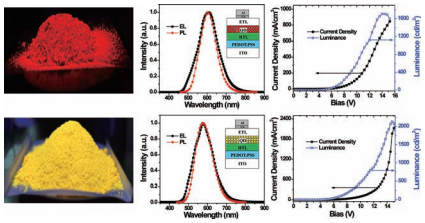

Highly emissive and color-tunable $CuInS_2$-based NCs are prepared by a combination of [Cu]/[In] molar ratio optimization, ZnS shell coating, and $CuInS_2$–ZnS alloying. The method is simple, hassle-free, and can be easily scalable to fabricate tens of grams of nanocrystal powders with photoluminescence quantum yields up to approximately 65%. Furthermore, the performance of high-quality $CuInS_2$-based NCs in electroluminescence devices is explored. These devices have lower turn-on voltages of around 5 V, brighter luminance, and improved injection efficiency compared to recent reports.

Magnetic Materials

Photoinduced Magnetization with a High Curie Temperature and a Large Coercive Field in a Co-W Bimetallic Assembly

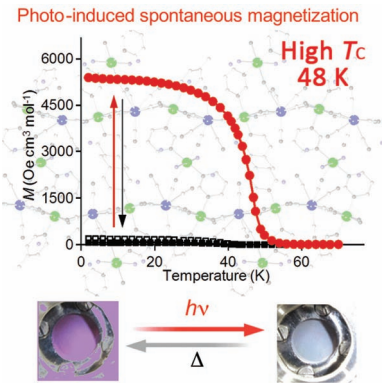

A 3D Co-W bimetal assembly with two types of aromatic molecules, $[\{Co^{II}(4\text{-methylpyridine})(pyrimidine)\}_2\{Co^{II}(H_2O)_2\}\{W^V(CN)_8\}_2]\cdot 4H_2O$, exhibits a photoinduced magnetization due to an optical charge-transfer-induced spin transition with a high Curie temperature (T_C) and a gigantic coercive field (H_c). The T_C and H_c values are the highest among photoinduced magnetic materials.

Shape-Memory Materials

Oligocrystalline Shape Memory Alloys

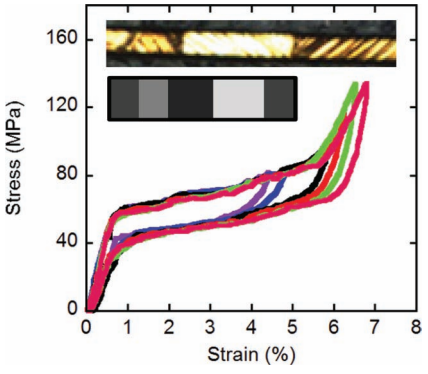

Oligocrystalline shape memory alloys are microstructurally designed shape memory alloy structures in which the total surface area exceeds the total grain boundary area. How the formation of an oligocrystalline grain architecture improves the performance of Cu-based, polycrystalline shape memory alloys to a point where their properties resemble those of single crystals is demonstrated.

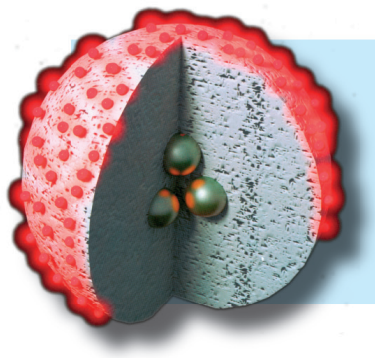

How to contact us:

Editorial Office:
Phone: (+49) 6201-606-235/531
Fax: (+49) 6201-606-500
Email: afm@wiley-vch.de

Reprints:
cherth@wiley-vch.de

Copyright Permission:
Fax: (+49) 6201-606-332
Email: rights@wiley-vch.de

FULL PAPERS

An all-acrylic thermoplastic elastomer swollen with a midblock-selective solvent behaves as a dielectric elastomer upon application of an electric field. The resultant electromechanical properties depend on polymer concentration. The optical images show the initial active area of a specimen and the same specimen at an electromechanical instability that promotes out-of-plane buckling.

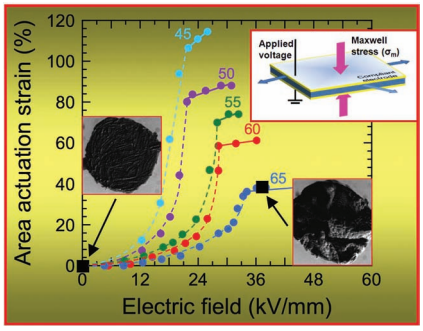

Elastomers

A site-selective substitution yields a single-phase defect-free perovskite. Magnetic measurements show no spin coupling and only a simple paramagnetic behavior. Magnetic anomalies are observed only for the samples with misplaced Mn, due to improper material processing and an unpredicted valence state of the Mn. This results in the formation of structural defects associated with the segregation and nucleation of magnetic species.

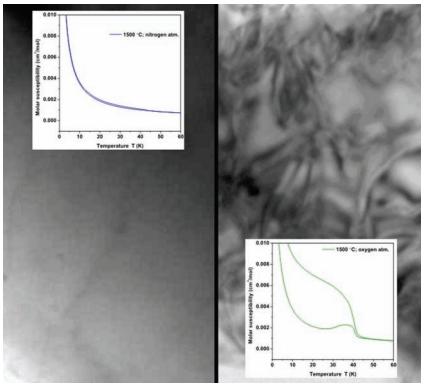

Magnetic Materials

Direct deposition of nanographene on oxides is achieved using an electron cyclotron resonance chemical vapor deposition (ECR-CVD) method. Wet etching and transfer are thus unnecessary, leaving the nanographene films free from metal impurities or polymer contamination. Spectroscopic analysis shows that a SiC layer appears at the interface between nanographene and SiO_2, highlighting the importance of carbide in the growth of graphene using oxides as catalysts.

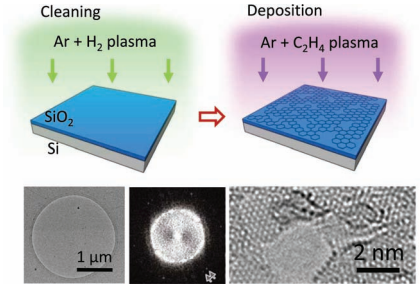

Graphene

A highly localized light-induced plasmon-assisted phase transformation of amorphous carbon nanostructures on noble metal surfaces (Au, Ag, Cu) is reported. This transformation results in the formation of a highly conductive carbon/metal interface with at least seven orders of magnitude lower electrical resistivity than the initial insulating interface.

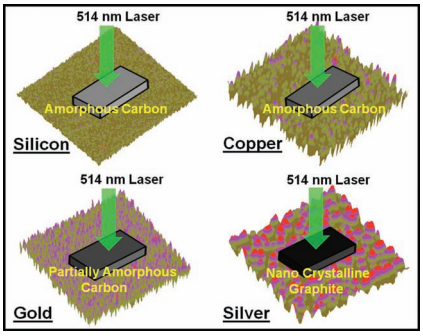

Carbon Nanostructures

CONTENTS

FULL PAPERS

Solid-State Batteries

By controlling and optimizing the formulation of a composite electrode, as well as the sintering parameters (temperature, pressure) that affect the compactness of both the electrolyte and the composite electrode, an efficient and safe solid-state Li-ion battery can be assembled in a one-step process by spark plasma sintering (SPS). The first prototype shows good cycling and a promising electrochemical performance.

Stimuli-Responsive Materials

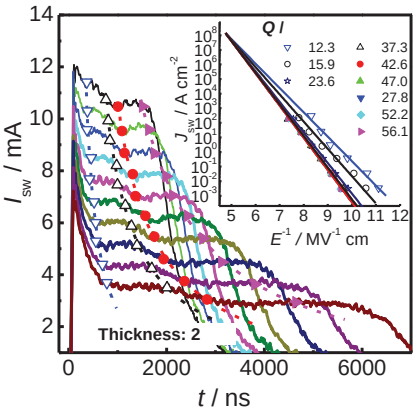

From domain switching current transients under pulses the field dependence of region-by-region domain switching currents from constant charge integrations across an inhomogeneous film area in $Pb(Zr_{0.35}Ti_{0.65})O_3$ thick films is estimated. An upper bound of the domain switching current density of 1.4×10^8 A cm^{-2} is extracted using a modified Merz equation. It is independent of film area and thickness, in support of nucleation rate-limited domain switching.

Stimuli-Responsive Materials

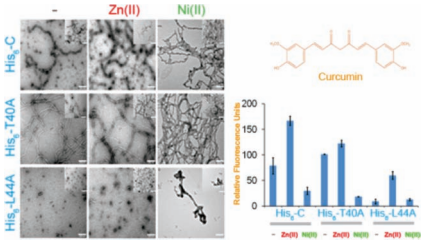

The impact of divalent metals on a cartilage oligomeric matrix protein coiled coil and two mutants with N-terminal hexahistidine tags is investigated. It is found that Zn(II) enhances the helical structure and stability of the protein while Ni(II) promotes macroscopic aggregation.

Solar Cells

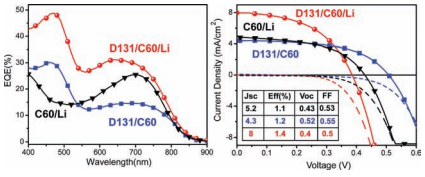

Hybrid solar cells based on a low band gap polymer infiltrated in TiO_2 mesoporous oxide are reported. The TiO_2/polymer interface is multiply functionalized with a fullerene-based self-assembled monolayer to drive efficient charge separation and with an organic dye to lead panchromatic photoresponse in the visible and near IR region and improved efficiency.

FULL PAPERS

Control of the degree of crystallinity and the preferred orientation of the perfluoro side chains, either parallel or perpendicular to the surface, is achieved by tuning the chemical vapor deposition (CVD) process parameters, i.e., initiator to monomer flow rate ratio, filament temperature, and substrate temperature. Low hysteresis and smooth films are obtained when the orientation of the perfluoro side groups is parallel to the surface.

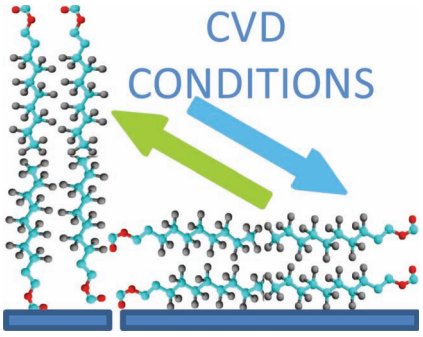

Thin Films

An anisotropic carbon nanotube (CNT)-polymer composite for bolometric applications in the mid-IR spectral range is studied. A responsivity that is the highest for CNT-based bolometers reported to date is shown. The flatness of the photoresponse in the broad spectral mid-IR range and enhanced responsivity provide the potential for the use of such novel composite materials for applications in IR spectroscopy and thermal imaging.

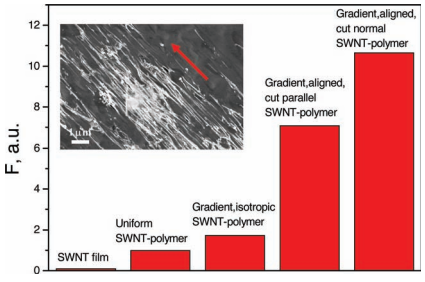

Carbon Nanotubes

A dihydronaphthyl-based C_{70} bisadduct ($NC_{70}BA$) is synthesized and explored as an acceptor in polymer solar cells. The solar cell based on poly(3-hexylthiophene) (P3HT):$NC_{70}BA$ shows a high open-circuit voltage and a high power conversion efficiency. The amorphous nature of $NC_{70}BA$ effectively suppresses the thermally driven crystallization, leading to high thermal stability of the P3HT:$NC_{70}BA$-based solar cell devices.

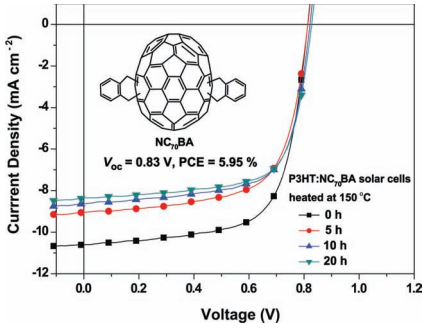

Solar Cells

Inverted devices with a dense and homogenous ZnO buffer layer derived from 0.1 M sol exhibit an overall conversion efficiency of 3.3%, which is a 32% increase compared to the power conversion efficiency of 2.5% for devices with a rough ZnO buffer layer made from 1 M sol. The results indicate that the efficiency of inverted polymer solar cells can be significantly influenced by the morphology of the buffer layer.

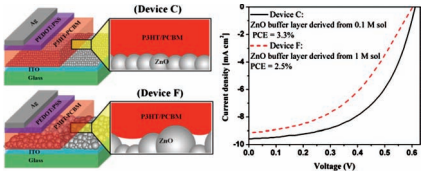

Solar Cells

FULL PAPER

Photovoltaic Devices

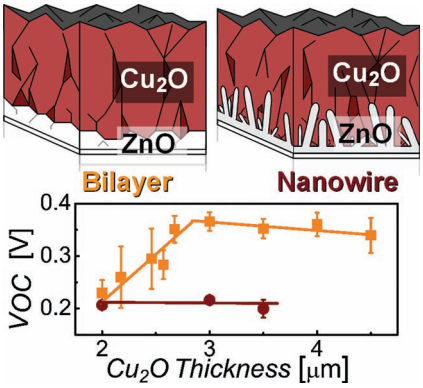

Electrodeposited bilayer and nanowire Cu_2O-ZnO photovoltaics are studied as a function of the Cu_2O absorber thickness, ZnO nanowire length, and nanowire seed layer. The low open-circuit voltage of nanostructured Cu_2O-ZnO cells is shown to result from an incompatibility between the desired nanostructure spacing and the Cu_2O thickness required to form the full built-in bias that inhibits recombination.